Graphene Boosts Thermoelectric Performance of a Zintl Phase Compound

SCHOLARONE™
Manuscripts

1   **Graphene Boosts thermoelectric Performance of a Zintl phase Compound**

2   A. Bhardwaj, A. K. Shukla, S. R. Dhakate and D. K. Misra*

3   CSIR-Network of Institutes for Solar Energy, Materials Physics & Engineering Division, CSIR-

4   National Physical Laboratory, Dr K.S. Krishnan Marg, New Delhi-110012

5   **Abstract:**

6   The concept of nanocomposites derived by incorporating a second minor phase in bulk

7   thermoelectric materials have established itself as an effective paradigm for optimizing the high

8   thermoelectric performance. In this work, this paradigm is for the first time extended to bulk

9   Zintl phase Mg_3Sb_2 and its isoelectronically Bi-doped derivative $Mg_3Sb_{1.8}Bi_{0.2}$ system. Herein,

10   we report the synthesis, microstructural details, electronic structure and thermoelectric properties

11   of (Mg_3Sb_2, $Mg_3Sb_{1.8}Bi_{0.2}$)/Graphene Nanosheets (GNS) nanocomposites with different mass

12   ratios. Field emission scanning electron microscopy (FE-SEM) and transmission electron

13   microscopy (TEM) investigation reveals that Mg_3Sb_2 nanoparticles are homogenously anchored

14   on the surface of GNS. We demonstrate that Mg_3Sb_2-based materials incorporated with small

15   content of graphene outperform optimally, resulting to a potential p-type thermoelectric

16   materials. The present nanocomposite additive of GNS deriving such a novel nanocomposites of

17   (Mg_3Sb_2, $Mg_3Sb_{1.8}Bi_{0.2}$)/GNS, enhances the electrical conductivity significantly, thereby

18   resulting a substantially large increase in the power factor. The enhanced electrical conductivity

19   of these nanocomposites is attributed to the increase in the carrier concentration and high carrier

20   mobility owed to the ultra high mobility of graphene. X-ray photoelectron spectroscopy (XPS)

21   core level spectra confirm weak bonding between GNS and Mg_3Sb_2. Increase in carrier

22   concentration is reflected in XPS valence band spectra and change in spectral weight near

23   valence band maxima is indicative of increased electrical conductivity in the nanocomposite

24   material. The thermal conductivity of these nanocomposites is noted to be reduced at high

25   temperature. These favorable conditions lead to enhanced thermoelectric figure-of-merit (ZT) ≈

26   0.71 at 773K for Mg_3Sb_2/GNS and a ZT ≈ 1.35 at 773 K for $Mg_3Sb_{1.8}Bi_{0.2}$/GNS nanocomposites

27   with the mass ratio of 80:1 which are ~170% and ~125% higher values compared to bare Mg_3Sb_2

28   and bare $Mg_3Sb_{1.8}Bi_{0.2}$ respectively. We strongly believe that the present novel strategy of

1   fabricating such nanocomposite of Zintl compound by utilizing, GNS, as a nanocomposite

2   additive, may provide an emerging path for improving thermoelectric properties of various Zintl

3   phase compounds.

4   *Corresponding author. E-mail address: misradk@nplindia.org, dakkmisra@gmail.com (DKM)

5

6   **Introduction**

7   The prospects of climate change, eventual fossil fuel depletion and increasing Co_2 content,

8   revive tremendous interest in exploring thermoelectric materials with high efficiency by which a

9   heat-to-electricity energy conversion could be accomplished. The efficiency of thermoelectric

10   energy conversion depends on material's dimensionless figure of merit ZT, defined as

11   $ZT = \frac{\alpha^2 \sigma T}{\kappa}$ [1] where σ is the electrical conductivity, α, Seebeck coefficient, κ, the thermal

12   conductivity and *T,* the absolute temperature. An efficient thermoelectric material requires high α

13   and σ and hence large power factor (PF= α^2 σ) as well as a low value of κ. A large value of

14   power factor of a material requires to possess large effective mass (m*) and high carrier mobility

15   μ.[2]

16   Several strategies such as doping,[3-6] solid solution alloying,[7-10] and nanostructuring-

17   nanocomposite,[11-16] have been utilized to modify the structure, hence improving the

18   thermoelectric properties. Such microstructural modifications lead to several important

19   mechanisms e.g. shifting of the Fermi level, creating local band resonant states, facilitating the

20   convergence of valence band or conduction bands, inducing high effective mass and interface

21   energy filtering effect which is usually helpful to improve the electronic properties.[17-21] Apart

22   from the improvement of electronic properties, these strategies are also helpful to impede the

23   propagation of thermal phonons by enhancing interface phonon scattering together with creating

24   local structural disorder to increase the frequency of phonon scattering processes as well. Based

25   on these strategies many materials such as Bi_2Te_3[22-26], LAST[27], TAGS[28], PbTe[29,30] SiGe[31,32] and

26   Zintl phase compounds[8,33-49] have been widely investigated and high ZT had been optimized.

27

28   All of the above strategies were mainly focused on increasing the m* and reducing the

29   lattice thermal conductivity. Unfortunately, the possibility to improve the carrier mobility (μ)

1 was missed by the researchers which had been largely the victim of such structural modifications

2 and hence needs to be focused for further improvement in thermoelectric properties.

3 Along the prospective to improve the electrical properties, graphene with high carrier

4 mobility (μ) can be utilized as composite additive for thermoelectric matrix in order to improve

5 the thermoelectric performance of resulting nanocomposites. Graphene has become one of the

6 most exciting material due to its unique electrical, optical, opto-electronics, and mechanical

7 properties. Graphene, particularly, with its two dimension (2D) single layer structure and with

8 sp^2 hybridization exhibits several intriguing properties e.g. high electrical conductivity ($\approx$

9 $6,000 Scm^{-1}$) high carrier mobility, ($\approx 20,000 cm^2 V^{-1} s^{-1}$) high specific surface area, ($\approx 2600 m^2 g^{-1}$)

10 and excellent mechanical properties (mechanical stiffness $\approx$ 130GPa).[50-56] These exciting

11 features of graphene make them a promising candidate for developing various kinds of

12 functional nanocomposites with potential applications in super capacitors[57,58], electric circuit[59],

13 fuel cell[60], conductive polymers[61] and bio-sensors[62]. Interestingly, it has been argued by some

14 researchers that the addition of graphene in Ag-matrix could increase the electrical conductivity

15 by introducing large number of electronic transmission channels.[63] However, till date; only few

16 reports[64-68] are available where graphene has been utilized as inclusions in thermoelectric

17 materials for optimizing their high ZT.

18 On the other hand, Zintl phases are considered as an unique class of thermoelectric

19 materials due to their unusual structural characteristics which lead to an important behavior of

20 phonon–glass electron–crystal (PGEC)[69] needed for a materials to achieve high ZT.[70,71] They

21 combine distinct regions of covalent bonding ideal for electron–crystal properties and ionically

22 bond cations that can be easily be substituted for precise tuning of electronic properties, leading

23 to the desired "electron crystal" behavior.[70,72] The complex structures create phonon–glass

24 properties resulting in low lattice thermal conductivity, making many Zintl compounds a natural

25 "phonon glass".[73,74] As a consequences of these behaviors, a varieties of Zintl phase compounds

26 such as $Yb_{14}MnSb_{11}$,[35] Zn_4Sb_3,[36] $Yb_9Mn_{4.2}Sb_9$,[37] filled skutterudites,[38,39] clathrates,[40,41]

27 $(Yb,Ba)Zn_2Sb_2$,[42,43] $YbCd_2Sb_2$,[44] $BaGa_2Sb_2$,[45] $(Eu_5,Yb_5)In_2Sb_6$,[46,47] $EuZn_2Sb_2$,[48] AZn_2Sb_2[49] etc.

28 with high ZT have been developed. However, the use of expensive rare earth elements and toxic

29 chalcogenides in majority of Zintl phase materials limits their use in large scale industrial

30 application for power generation.

1   Mg_3Sb_2 is a unique Zintl phase compound constituted with cheap, rare earth free and

2   non-toxic constituents which crystallizes in cubic bixbyite (α-phase) as well as in hexagonal

3   structures (β-phase).[75] The α-phase cubic bixbyite structure is La_2O_3–type which is the high

4   temperature phase, structured with 80 atoms per unit cell with 48 Mg and 32 Sb atoms. At low

5   temperature, below ~1200K, Mg_3Sb_2 crystallizes to Mn_2O_3 type β-phase with unit cell composed

6   of 5 atoms (3 Mg and 2 Sb). The β-phase hexagonal structure (Space group $P\bar{3}ml$; No. 164)

7   which is under our investigation, consists of two inequivalent Mg sites, denoted as Mg(I) and

8   Mg(II) which are covalent and ionic in nature respectively. Thus, the bonding characteristic of

9   Mg_3Sb_2 is in between metallic and ionic.[76,77] Similar to the structure of $CaAl_2Si_2$, the

10   stoichiometric Mg_3Sb_2 compound consists of interspersed $Mg_2Sb_2^{2-}$ layers (the tetrahedral

11   position in the lattice) and Mg^{2+} cation layers (the octahedral position in the lattice).[78] The β-

12   Mg_3Sb_2 phase exhibits a band gap of 0.4 eV. It has a fairly large effective mass, high thermo

13   power, low thermal conductivity but unfortunately a poor electrical conductivity which is largely

14   the reason for the low thermoelectric performance. In our earlier report[8], we demonstrated the

15   increase in ZT in $Mg_3Sb_{2-x}Bi_x$ ($0 \leq x \leq 0.4$) alloys by isoelectronic substitution of Bi^{3-} on Sb^{3-}

16   site. The enhancement in ZT was attributed to the increased Seebeck coefficient and reduced

17   thermal conductivity. Despite the large increase in the Seebeck coefficient and significant

18   reduction in the thermal conductivity, there was no significant improvement in the electrical

19   conductivity resulting to only moderate improvement in ZT of these materials.[8]

20   In this work, we have adopted nanocomposite approach by incorporating graphene

21   nanosheet (GNS), in Mg_3Sb_2 (with high m* and low κ) for further improving the ZT of this

22   potential thermoelectric material. Combination of higher μ and lower κ would be important to

23   attain superior thermoelectric performance. Several exciting features of graphene namely high

24   electrical conductivity and a large carrier mobility perceived with potential Mg_3Sb_2

25   thermoelectric materials may be expected to result in large increase in the electrical conductivity

26   with less effect on the Seebeck coefficient of Mg_3Sb_2/GNS nanocomposite which is expected to

27   improve the thermoelectric properties.

28   Herein, we have synthesized Mg_3Sb_2/GNS nanocomposite by incorporating GNS in

29   different weight fractions in a precursor of pre-synthesized Mg_3Sb_2 host compound via wet ball

1 milling route followed by rapid-heating using spark plasma sintering (SPS). An enhanced

2 thermoelectric figure-of-merit (ZT) ≈ 0.71 at 773 K of Mg_3Sb_2/GNS with mass ratio of 80:1 for

3 nanocomposite was realized which is about 170% higher than that of its bulk counterpart Mg_3Sb_2

4 compound. Further, the same strategy of fabricating the nanocomposite by incorporating GNS

5 with the same mass ratio of 80:1 was demonstrated in $Mg_3Sb_{1.8}Bi_{0.2}$ and thermoelectric

6 properties were investigated. Interestingly, GNS addition consistently enhances the electrical

7 conductivity (>650%) which in turn increases the power factor (~90%) and thereby resulting to a

8 large increase in ZT ≈ 1.35 at 773K of $Mg_3Sb_{1.8}Bi_{0.2}$/GNS nanocomposite with mass ratio of

9 80:1. To the best of our knowledge, such strategy of incorporating GNS in Zintl phase

10 thermoelectric matrix for achieving high thermoelectric figure of merit has not been reported so

11 far.

12 **2.0. Experimental Detail**

13 **2.1 Materials Processing and Densification**

14 Stoichiometry of Mg_3Sb_2 and $Mg_3Sb_{1.8}Bi_{0.2}$ with high purity elements magnesium (Mg; 99.99%,

15 Alfa Aesar), antimony (Sb; 99.99%, Alfa Aesar), and bismuth (Bi; 99.99%, Alfa Aesar), were

16 blended by mechanical milling and subsequently grounded in an agate mortar. The blended

17 powders were then subjected to spark plasma sintering (SPS) at a temperature and pressure of

18 1073 K and 50 MPa, respectively, for a holding time of 10 min. Pellets of 12.7 mm in diameter

19 were obtained. The strategy to following the SPS synthesis route is to melt the stoichiometric at

20 high temperature and cool it fast to form nanosized grains of single Mg_3Sb_2 composition phase.

21 The graphite intercalated compound was thermally expanded to get fully thermally

22 expanded graphite[79]. The thermally expanded graphite and organic solvent dimethyl formamide

23 (DMF) was taken in the ratio of 5.0 mg/ml and was placed into a stainless steel jar containing

24 stainless steel balls of diameter 5 mm. The ratio of expanded graphite to stainless steel ball was

25 1:100 by weight. The milling was carried out in an ambient temperature. The mixture was milled

26 by planetary ball milling for 15 hours at a rotation speed 300 rpm. The resulting solution was

27 dried and few layer graphene (FLG) nano sheets (GNS) in the form of powder were obtained[80].

28 The FLG nano sheets derived from the ball milling of expanded graphite in organic solvent was

29 used as conducting reinforcement in the pre-synthesized precursor of Mg_3Sb_2. Before mixing of

1 graphene in Mg_3Sb_2 matrix, it was ball milled for two hours to disperse the GNS properly. The

2 different mass ratio 100:1, 80:1, 60:1 and 40:1 of Mg_3Sb_2/GNS were mixed in wet ball milling in

3 organic solvent and subsequently the organic solvent was evaporated completely. The resulting

4 mixtures of Mg_3Sb_2 and GNS were subjected to SPS at temperature of 600 °C and pressure of 50

5 MPa in order to have a pellet of high density nanocomposite materials. The similar synthesis

6 procedure was followed for fabricating $Mg_3Sb_{1.8}Bi_{0.2}$/GNS nanocomposite with mass ratio of

7 80:1.

8 **2.2 Structural Characterization**

9 The gross structural characterization of Mg_3Sb_2/GNS nanocomposite was carried out by powder

10 X-ray diffractometer (Rigaku Mini Flex II) in reflection θ- 2θ geometry, with position sensitive

11 detector (Ultafast D Tex), operating at 30 kV and 20 mA, using a graphite monochromator and

12 CuK_α radiation with wavelength λ ≈ 1.5406 Å along with $CuK_{\alpha2}$ filter and rotating anode

13 equipped with powder 2θ diffractometer ranging from 20 to 80 degrees. The experimental

14 conditions and parameters such as sample size, power ratings of X-ray tube (30 kV, 20 mA) and

15 other diffractometer parameters such as scan speed, counting steps etc. were kept constant for all

16 diffraction experiments.

17 The microstructure investigation of host Mg_3Sb_2 Zintl compound and Mg_3Sb_2/GNS

18 nanocomposite after SPSed was carried out by field emission scanning electron microscopy (FE-

19 SEM; Model: SUPRA40 VP, operating at 30kV) and HRTEM (Modell: Technai G^2F^{30};STWIN)

20 operating at 300 kV. The elemental analysis of the samples was performed using energy

21 dispersive spectroscopy (EDS) attached to the FE-SEM. The detail of TEM specimen

22 preparation of Mg_3Sb_2 has been described elsewhere[8] and same procedure has been followed for

23 present nanocomposites.

24 **2.3 Thermoelectric Properties**

25 Thermal diffusivity of $(Mg_3Sb_2,\ Mg_3Sb_{1.8}Bi_{0.2})$/GNS nanocomposite samples were measured by

26 using a laser flash system (Lineseis, LFA 1000) on disk-shaped thin specimens with approximate

27 thickness of 1.5 mm and diameter of 12.7 mm. The disc specimens used for thermal diffusivity

28 were sprayed with a layer of graphite in order to minimize errors due to emissivity. Specific heat

was determined by a differential scanning calorimetry (DSC) instrument (822e Mettler Toledo). The thermal conductivity of nanocomposites was calculated using the relation, $\kappa = d \times Cp \times \rho$ where d is the thermal diffusivity, ρ the geometrical pellet density and Cp the heat capacity. The Seebeck coefficients and the resistivity were measured simultaneously employing commercial equipment (ULVAC, ZEM3) over the temperature range of 300 K to 773 K on samples of polished bars of about $3 \times 1.5 \times 10$ mm^3.

2. 4. Raman Spectroscopy

The graphene derived from expanded graphite and Mg_3Sb_2/GNS nanocomposites was characterized by Raman spectrometer (Reninshaw, micro Raman model in Via Reflex) with 514 nm laser excitation and notch filter cutting at 50cm^{-1} at room temperature. The Raman spectra was recorded from 50 cm^{-1} to 3000 cm^{-1} with 5 mW laser power and 10s exposure time. The 50 X microscope objective was used and the spot size of the laser was 1-2 μm.

2.5. Hall measurement

Room temperature Hall Effect was carried out using the van der Pauw method. The Hall coefficient was determined using an a.c. power supply of 29 Hz frequency and magnetic induction of 0.9 T. The Hall carrier concentration n_H was calculated via $n_H = 1/eR_H$, where R_H is the Hall coefficient and e is the electron charge. The Hall mobility μ_H was calculated by a relation $\mu_H = \sigma/n_He$, where σ is the electrical conductivity.

2.6. Thermal Expansion measurement

The coefficient of thermal expansion (CTE) of GNS, Mg_3Sb_2, Mg_3Sb_2/GNS nanocomposites was measured by thermo-mechanical analyzer (TMA-Q400, TA Instrements) in Nitrogen atmosphere in the temperature range 50-500 °C@10 °C /min.

2. 7. X-Ray Photo Electron Spectroscopy (XPS)

XPS experiments were carried out in a multi-chamber equipped with an Omicron EA 125 electron energy analyzer and monochromated Al K$_\alpha$ X-ray source with ultra high vacuum (UHV) surface science system maintained at the base pressure of 10^{-10} mbar range. All binding energies

1   have been referenced to the Fermi edge of an Ar^+ sputtered clean polycrystalline Ag sample. The

2   XPS data has been collected using 20 eV analyzer pass energy which results in an overall energy

3   resolution of 0.37 eV determined from the Fermi edge broadening of polycrystalline Ag. The

4   composition of the samples have been determined from the normalized area under the curve of

5   Mg 2s and Sb 4d core levels of Mg_3Sb_2 and Mg 2s, Sb 4d, and graphene core levels for

6   Mg_3Sb_2/GNS nanocomposite. These spectra are recorded under similar conditions, i.e.

7   comparable analyzer settings, x-ray source intensity and sample position. Area under the curve

8   of each core level used in composition calculation was normalized by respective photoemission

9   cross section, inelastic mean free path and analyzer transmission function.

10   **3. Results and Discussion**

11   The X-ray diffraction (XRD) pattern of the SPSed pellets of Mg_3Sb_2, (Mg_3Sb_2,

12   $Mg_3Sb_{1.8}Bi_{0.2}$)/GNS nanocomposites are shown in Figure 1(a).

13   In case of bare Mg_3Sb_2 compound, all the peaks are well indexed to β-Mg_3Sb_2

14   (hexagonal; space group P -3m1, JCPDS no. 00-003-0375) with no detectable impurities of other

15   phases (The inset shows the crystal structure of Mg_3Sb_2). On the other hand, XRD of all the

16   nanocomposites reveal the presence of graphene peak (at $2\theta\approx26.51^\circ$) along with prominent peaks

17   of β-Mg_3Sb_2. The intensity of graphene peaks increases consistently with increasing

18   concentration of GNS in the Mg_3Sb_2. Fig 1 (b) displays TEM images of GNS revealing the GNS

19   width to be about ~ 260 nm. The inset of fig. 1(b) is XRD pattern of GNS showing peaks of

20   graphene. No any impurity phase was detected. The HRTEM images obtained from graphene

21   [fig. 1(c)] clearly reveals the lattice fringes corresponding to graphene.[81]

22   Figure 2 shows the Raman spectra of GNS, Mg_3Sb_2 and Mg_3Sb_2/GNS nanocomposite

23   for mass ratio 80:1. The Raman spectra recorded from graphene reveals three bands at 1354,

24   1582 and 2723 cm^{-1} corresponding to the disordered (D) band, graphitic (G) band and broad 2D

25   band respectively. The disordered (D) band is due to the sp^3 bonding of carbon atoms, graphitic

26   (G) band is due to the sp^2 bonding of carbon atoms and broad 2D band which is the second order

27   of the D peak but it is not related to defect level in the structure. The intensity ratio of 2D/G is

28   ~0.50 which corresponds to four to five layers in the graphene. However, for the Mg_3Sb_2:GNS

1 nanocomposite with mass ratio 80:1, same Raman shift D, G and 2D peaks are appearing with

2 2D/G ratio of ~0.50 together with spectra consisting of peak at 114 and 156 cm^{-1} which

3 corresponds to Mg_3Sb_2. Thus, the peaks of graphene and Mg_3Sb_2 for nanocomposites indicate

4 that both phases coexist. The Raman spectra of bare Mg_3Sb_2 (as shown in inset; fig. 2) consists

5 of only two peaks at 118 and 147 cm^{-1}. However, in case of nanocomposite Mg_3Sb_2/GNS (80:1),

6 there is a little shift to the lower side as compared the Raman shifts of Mg_3Sb_2. This is due to the

7 coexistence of Mg_3Sb_2 and GNS in the nanocomposite. It can be noted that the Raman spectra

8 only provide the statistical average of the powder sample, where a huge number of graphene

9 sheets in single-, double- or few layered forms coexist. Thus, graphene can be distinguished as

10 three different layers such as single, double, and few layers in more generalized way as

11 suggested by Geim et al.[82] and hence practically the graphene in Mg_3Sb_2/GNS nanocomposite

12 can be regarded as " graphene" in the form of few layered.

13 The coefficient of thermal expansion (CTE) can give the idea of dimensional changes

14 occurred in nanocomposites with increasing temperature at defined load. It also gives the idea of

15 bonding between the reinforcing constituent in the nanocomposites. The linear CTEs of the

16 GNS, Mg_3Sb_2 and Mg_3Sb_2/GNS nanocomposites pellets were measured in the temperature range

17 50-500ºC. A high value of CTE of 310.5 x 10^{-6} ºC^{-1} in case of GNS pellet was observed, which is

18 due to poor bonding between the few layer graphene suggesting a linear shrinkage in the pellet

19 with increasing temperature and as a consequence thermal stresses exert on the few layer

20 graphene. On the other hand, in case of matrix Mg_3Sb_2 a reasonably small value of CTE ~18.96

21 x 10^{-6} ºC^{-1} was revealed resulting a strong bonding between constituent which arrest the

22 shrinkage with increasing temperature. Interestingly, in case of Mg_3Sb_2/GNS nanocomposites,

23 the CTE ~23.46 x 10^{-6} ºC^{-1} was observed, which is slightly larger than the CTE of the bare

24 Mg_3Sb_2 matrix indicating a weak bonding between GNS and Mg_3Sb_2.

25 We have earlier reported the detailed electronic structure study of bare Mg_3Sb_2 using XPS

26 core level and valence band spectra.[8] Here, we have employed the XPS to compare the electronic

27 structure of bare Mg_3Sb and Mg_3Sb_2/GNS nanocomposites. Figure 3 show XPS survey spectra of

28 bare Mg_3Sb_2, GNS and Mg_3Sb_2/GNS nanocomposites over wide binding energy (BE) range.

29 Spectrum of GNS (bottom) shows the presence of only carbon related features and absence of O

1   1s and any other feature verifies the purity of GNS. It can be noted that finite amount of O 1s

2   signal in XPS survey spectrum of GNS has been reported in several recent reports of GNS

3   synthesis using different routes.[83-85] Usually GNS samples are obtained by the reduction of

4   graphite oxide (GO) and it is not always possible to reduce the attached oxygen functional group

5   completely which is detrimental to the electrical properties of graphene. However, in our case,

6   almost complete absence of O 1s signal indicates the effectiveness of used synthesis procedure in

7   removing oxygen functional group.

8   Survey spectrum of bare Mg_3Sb_2 (top) also confirms the purity of the materials as we only

9   see the Mg and Sb related features.[8] We clearly observe the emergence of C 1s signal in the

10   Mg_3Sb_2/GNS nanocomposites. The C 1s signal increases with increasing mass ratio of GNS

11   which is the evidence of increasing inclusion of GNS in the nanocomposite samples for larger

12   mass ratio of GNS. We have observed the inclusion of GNS in all nanocomposite samples

13   reported here by the presence of C 1s signal (spectra not shown here). We have mainly focused

14   our XPS analysis on Mg_3Sb_2/GNS (80:1) sample as it performs best among other

15   nanocomposites reported here.

16   We have acquired the high resolution C 1s XPS core level spectra to confirm the quality of

17   GNS and to identify the presence of any other functional group attached with it. C 1s core level

18   for GNS has been fitted using six Gaussian-Lorentzian components using a least χ^2 iterative

19   program after Shirley background subtraction (Fig. 4, bottom spectra).

20   The individual deconvoluted components (shaded region) correspond to different functional

21   groups attached with C as identified in the Fig. 4 (graphitic sp^2 C=C at 284.55 eV, sp^3 C-C at

22   284.95 eV, C-O at 286.2 eV, C=O at 287.3 eV, O-C=O at 288.6 eV and $\pi - \pi^*$ shakeup feature

23   at 290.5 eV BE). Relative percentages of C=C, C-C, C-O, C=O, O-C=O are found to be 56, 29,

24   10, 4 and 1 respectively. Experimental uncertainty in BE position is 0.05 eV and ±5% of base

25   value for determining the percentage. Full width at half maximum (FWHM) of C=C component

26   turns out to be 0.6 eV and it varies between 1 – 1.15 eV for other C-functional group

27   components. Energy position and FWHM of sp^2 C=C and other components is in good

28   agreement with earlier reports based on the analysis of C 1s of a few layer graphene (FLG) and

29   GNS.[83,84,86-88] Presence of dominating sp^2 C=C establishes the graphene nature of our GNS.

1   Similar fitting routine as of GNS has been applied to C 1s core level spectrum of Mg_3Sb_2/GNS

2   (80:1). It is clearly evident from nanocomposite material related C 1s fitting that graphene nature

3   of GNS is preserved in nanocomposite Mg_3Sb_2/GNS (80:1). We observe slight increase in C-

4   C/C-OH component in Mg_3Sb_2/GNS (80:1) compared to GNS and it could be attributed to the

5   synthesis procedure of nanocomposites (wet chemical synthesis followed by further milling and

6   SPS).

7   The Mg 1s and Sb 3d core level spectra for bare Mg_3Sb_2 and nanocomposite Mg_3Sb_2/GNS

8   (80:1) are shown in figure 5. We do not observe any appreciable change in the BE position and

9   line shape of core levels between bare and nanocomposite samples. It suggests that bonding

10   between GNS and Mg and Sb is either nonexistent or very weak. This observation is also in good

11   agreement with our thermal expansion measurements which suggest loose bonding between

12   GNS and Mg_3Sb_2.

13   We have compared the XPS valence band (VB) spectra of bare Mg_3Sb_2 and nanocomposite

14   Mg_3Sb_2/GNS (80:1) as presented in Fig. 6. The VB is composed of mainly two features; main

15   peak around 2 eV BE and another peak at around 4.6 eV BE. These peaks are made up of Sb 5p

16   states hybridized with Mg 3s states with dominant character of Sb 5p.[8] No significant change in

17   energy positions or relative intensities of main features is observed between bare and composite

18   material which also confirms the weak chemical interaction between Mg_3Sb_2 and GNS as

19   observed in core level spectra (Fig. 5). Near E_F energy region is shown in inset of Fig. 6. We

20   have determined the position of valence band maxima (VBM) from the cross-section of two

21   straight line fits.[8] We observe the small change in the BE position of VBM between bare Mg_3Sb_2

22   (0.4 eV) and nanocomposite Mg_3Sb_2/GNS (0.34 eV) with mass ratio 80:1 due to increase in p-

23   type carriers in composite compared to bare Mg_3Sb_2. We also observe the small increase in the

24   spectral weight near VBM (shown as patterned part) for composite material compared to bare

25   Mg_3Sb_2 and it may be related to the increased electrical conductivity in Mg_3Sb_2/GNS

26   nanocomposite.

27   In order to confirm the phase purity at macroscopic scale, homogeneities and compositional

28   analysis of SPSed pellet of bare Mg_3Sb_2 and Mg_3Sb_2/GNS nanocomposites samples were

29   performed by FE-SEM and HRTEM. The homogeneities of SPSed samples in bare Mg_3Sb_2 and

Mg$_3$Sb$_2$/GNS nanocomposites for mass ratios 100:1; 80:1, 60:1 and 40:1 were assessed by averaging the compositions obtained by energy dispersive x-ray analysis (EDAX) at 5 different regions of each sample. The average value of composition is shown in table 1 marked as SEM-EDAX compositions. All the samples were found to be macroscopically homogeneous as revealed by SEM-EDAX analysis given in table 1. Figure 7 shows FE-SEM morphologies of bare Mg$_3$Sb$_2$ and Mg$_3$Sb$_2$/GNS nanocomposite with mass ratio 80:1.

The SEM image of SPSed bare Mg$_3$Sb$_2$ (Fig 7a) sample clearly reveals the homogeneous polycrystalline grains. Energy dispersive X-ray spectrum shown in Fig 7(b) qualitatively reveals the presence of Mg and Sb without any minor impurities. The quantification data obtained from EDAX results to the composition of Mg$_3$Sb$_2$ phase. Figure 7(c-f) display FE-SEM morphologies of SPSed Mg$_3$Sb$_2$/GNS nanocomposite sample with mass ratio 80:1. The Mg$_3$Sb$_2$ particles appear to be uniformly confined on the surface of GNS as shown in Fig 7(c). It is interesting to note that the Mg$_3$Sb$_2$ particles in the nanocomposite sample (the particle size ranging from 2.0 nm to 50 nm) are significantly smaller than the particles in bare Mg$_3$Sb$_2$ (the particle size ranging from 100 nm to 500 nm). In order to see the consistent behavior of graphene introduction on reducing the size of Mg$_3$Sb$_2$ particle, SEM measurements were conducted on all the nanocomposites with mass ratio 100:1, 60:1 and 40:1 which are shown in supplementary information S1. All of the nanocomposite samples show smaller particle size of Mg$_3$Sb$_2$ and decreases with increasing GNS concentration. Thus, we believe that graphene refined the size of Mg$_3$Sb$_2$ particles and generates reduced grain boundaries upon the formation of nanocomposites similar to the other reports for many other systems.[64-68] Obviously, the graphene in Mg$_3$Sb$_2$ matrix prevents the growth of grain boundary. The SEM-EDAX analysis (Fig 7e) clearly reveals the presence of Mg$_3$Sb$_2$ with graphene. The EDAS-mapping and line scan upto large region of sample were also probed on this nanocomposite samples to find the presence of any minor impurities other than Mg, Sb and C. Evidently, no impurities other than constituents of the nanocomposite were observed, showing the purity of the nanocomposite material.

The TEM investigation of SPSed Mg$_3$Sb$_2$ sample was carried out to check the purity of sample before it can be deployed to fabricate the nanocomposite materials. Figure 8(a) presents bright field image of Mg$_3$Sb$_2$ showing a polycrystalline sample with sizes ranging from 100nm to

1   500nm. A corresponding selected area electron diffraction pattern (SAEDP) shows a set of

2   Debye rings with fine sharp spots overlapping on individual rings (Fig. 8b) confirming the

3   material to be β-Mg_3Sb_2 hexagonal crystal structure (Sapce group $P\bar{3}ml$.). Several lattice scale

4   images (Fig. 8c) were recorded revealing different orientation of Mg_3Sb_2 and excellent

5   crystallinity of the samples was realized. EDS analysis [Fig. 8(d)] clearly reveals the elemental

6   Mg and Sb peaks with composition very close to the nominal Mg_3Sb_2.

7   Figure 9(a) represents a typical bright field electron micrograph of SPSed Mg_3Sb_2/GNS

8   nanocomposite sample with mass ratio 80:1 showing the Mg_3Sb_2 particles with sizes ranging

9   from 2.0 nm to 50 nm which is much smaller than the sizes of bare Mg_3Sb_2. Obviously, the

10   Mg_3Sb_2 particles are found to be anchored on the surface of graphene nano sheets. The decrease

11   in the sizes of Mg_3Sb_2 particles in Mg_3Sb_2/GNS nanocomposites indicates that the GNS in

12   Mg_3Sb_2 matrix suppresses the growth of the grain boundaries which is consistent with our SEM

13   investigation.[64-68] The presence of GNS can easily be discerned in Fig 9(b & c) as the lattice

14   fringes corresponding to GNS can be clearly identified. The HRTEM shown in the inset of Fig.

15   9(c) clearly shows both phases with orientational relationship (002)GNS // (101)Mg_3Sb_2. Figure

16   9(d) displays HRTEM image showing only Mg_3Sb_2 grains, no GNS was resolved at such high

17   magnification. This could be due to either the microscopic condition are not optimal or depth of

18   focus for the two phases were different to be detected simultaneously. Figure 9(f) shows the

19   schematic reaction mechanism for the formation of Mg_3Sb_2/GNS nanocomposite.

20   In order to understand the impact of such novel fabricated nanocomposite with graphene as

21   nanocomposite additive on the thermoelectric performance of bare undoped and Bi doped

22   Mg_3Sb_2, all the nanocomposites have been subjected to thermal and electronic transport

23   measurements. The electronic and thermal transport properties of all the nanocomposites have

24   been compared with the parent Mg_3Sb_2 material. Figure 10 displays the temperature dependence

25   of electrical conductivityσ, of Mg_3Sb_2/GNS nanocomposite for different mass ratios.

26   The electrical conductivity of all the nanocomposites increased with rising temperature

27   displaying semiconducting behavior. Moreover, regardless of the temperature, electrical

28   conductivity increases monotonously with increasing GNS concentration and reaches its

29   maximum value for the nanocomposite with mass ratio 40:1. The various room temperature

1   physical properties are shown in table 1. The Mg_3Sb_2/GNS nanocomposites exhibit an increased

2   electrical conductivity compared to bare Mg_3Sb_2 over the entire temperature range. The electrical

3   conductivity σ can be expressed by a relation as

$$\sigma = ne\mu$$

4   Where n is the carrier concentration, e is the charge of an electron and μ is the carrier mobility.

5   Thus the enhancement in the electrical conductivity for Mg_3Sb_2/GNS nanocomposites may be

6   attributed to either increase in carrier concentration, or an increase in carrier mobility. The table

7   1 clearly demonstrates the increasing n and μ with increasing GNS concentration. The maximum

8   carrier concentration and mobility was observed for the Mg_3Sb_2/GNS nanocomposite with mass

9   ratio 40:1. For example, n = 7.3×10^{20} cm^{-3} and μ = 144 cm^{2}V^{-1}s^{-1} for the nanocomposite with

10   mass ratio 40:1, which is much higher than that of bare Mg_3Sb_2 (n = 1.1×10^{20} cm^{-3} and μ = 11

11   cm^{2}V^{-1}s^{-1}). A systematic increase in the mobility was noticed in all the nanocomposites. Thus

12   such a significant increase in the electrical conductivity is attributed primarily due to significant

13   increase in μ and moderate increase in n. The rationale for this is that the pristine few layered

14   graphene reveals p-type thermoelectric properties and the graphene with its unique 2D planar

15   structure has ultra high electron mobility (more than 20,000 cm^{2}V^{-1}s^{-1}).[45] It has been suggested

16   that the graphene in the nanocomposite may supply large number of extra transmission channels

17   for electrons[58] to take part in the transport which significantly improves the electrical

18   conductivity. We speculate that same phenomenon would have taken place in the present

19   nanocomposites. It is worth mentioning that the explanation why graphene enhances ultrahigh μ

20   and significantly larger σ is entirely plausible and exact physical mechanism still requires further

21   investigation.

22   The temperature dependent Seebeck coefficients for bare Mg_3Sb_2 and Mg_3Sb_2/GNS

23   nanocomposites are shown in Fig 11(a). The Seebeck coefficient of all the nanocomposites is

24   positive in the whole temperature range, indicating that majority of the carriers are holes which is

25   consistent with the Hall measurement.

26   With the introduction of GNS, the Seebeck coefficients at room temperature decrease for all

27   the nanocomposites and maintained such decrement throughout the whole temperature range as

1   compared to that of bare Mg_3Sb_2. The decrease in Seebeck coefficient at room temperature is

2   consistent with associated increase in carrier concentration. This phenomenon of inverse relation

3   between α and σ can be explained by the equation, [65,89,90]

$$\alpha = \pm \frac{k_B}{e}\left[2 + ln\frac{2(2\pi m^* k_B T)^{\frac{3}{2}}}{h^3 n}\right]$$

4   Where m* is the effective mass relating the density of states and n, the carrier concentration. As

5   noted above, the introduction of GNS induces large carrier concentration and hence according to

6   the equation, the α is reduced. The absolute values of Seebeck coefficients of both bare Mg_3Sb_2

7   and Mg_3Sb_2/GNS nanocomposite increase with temperature and attain a peak values at a certain

8   temperature, and then further followed by a decreasing trend at higher temperature. This can be

9   accounted to an increased number of thermally excited minority carriers at higher temperature

10   leading to decreased Seebeck coefficient. Figure 11(b) displays the power factor (PF=$\alpha^2\sigma$) of

11   bare Mg_3Sb_2 and Mg_3Sb_2/GNS nanocomposites. The nanocomposites exhibit higher power

12   factor compared to bare Mg_3Sb_2 which is mainly ascribed to the increased σ due to introduction

13   of GNS in the Mg_3Sb_2 matrix. The highest power factor was optimized for the Mg_3Sb_2/GNS

14   nanocomposites with mass ratio of 80:1 at 673 K. The maximum power factor for this

15   nanocomposite was realized to be 4.5 x 10^{-4} W/mK^2 at 673K which is 130% larger than the bare

16   Mg_3Sb_2 (PF= 1.98 x 10^{-4} W/mK^2). The optimized higher power factor of Mg_3Sb_2/GNS with mass

17   ratio: 80:1 was resulted due to a large increase in the electrical conductivity (~600% larger value

18   than bare Mg_3Sb_2). Thus incorporation of graphene in Mg_3Sb_2 thermoelectric matrix is beneficial

19   by increasing the electrical conductivity while inducing less effect on the Seebeck coefficient

20   which in turn increases the large power factor (PF= α^2 σ).

21   In addition to α and σ, the thermal conductivity, κ is also an important parameter for

22   thermoelectric material. Figure 12(a) displays the temperature dependence of thermal

23   conductivity κ (T) of bare Mg_3Sb_2 and Mg_3Sb_2/GNS nanocomposites. The incorporation of GNS

24   into Mg_3Sb_2 leads to increased thermal conductivity and increases with increasing GNS content.

25   For instance, the total thermal conductivity (κ= 2.4 W/mK) of Mg_3Sb_2/GNS nanocomposite for

26   higher GNS concentration, say for 40:1 is much larger than that of Mg_3Sb_2 (κ= 1.39 W/mK).

This could be attributed to significant contribution from electronic part which could have been induced by GNS inclusions. The temperature dependent thermal conductivity of bare Mg_3Sb_2 and all the nanocomposites Mg_3Sb_2/GNS decrease with temperature, which indicates that the phonon conductivity dominates. Interestingly, the nanocomposite Mg_3Sb_2/GNS with mass ratio 80: 1 displayed a low thermal conductivity at high temperature than the bare Mg_3Sb_2 which is reduced by 15% of the value of bare Mg_3Sb_2 at high temperature. The lattice thermal conductivity [Fig. 12 (c)] including bipolar was obtained by subtracting the electronic thermal conductivity from the total measured thermal conductivity. The Wiedemann-Franz law has been used to calculate the electronic thermal conductivity ($\kappa_e = L\sigma T$, where L is Lorenz number, σ, the electrical conductivity and T, the temperature in K). Here, we use the temperature dependent Lorenz number[91] and the bipolar contribution was taken into account by assuming $\kappa_{lattice} \sim 1/T$[92] Figure 12(c) represents the temperature dependent lattice thermal conductivity. The lattice thermal conductivity of all the samples was observed to decrease with increasing temperature (Fig. 12c), showing similar falling trend in the total thermal conductivity. The lattice thermal conductivity ($\kappa_L = 0.34$ W/mK) of Mg_3Sb_2/GNS nanocomposite at 773K is much smaller than the thermal conductivity ($\kappa_L = 0.54$ W/mK) of Mg_3Sb_2 at 773K. However, a higher $\kappa_{lattice}$ for all the nanocomposites than their respective counterparts were noted at low temperature, which might be resulted due to large lattice thermal conductivity of graphene. The rationale behind this observation could be understood by considering the properties of graphene.

The graphene has large specific surface area apart from large $\kappa_{lattice}$ and hence, an inverse effect of graphene on the thermal conductivity may also be expected. However, we anticipate that large lattice thermal conductivity is observed due to later i.e. due to high lattice thermal conductivity of graphene. The large surface area of graphene providing more interfaces to scatter phonons may not be sufficient to dominate over the large lattice thermal conductivity due to graphene addition, which needs to be further investigated. The electronic thermal conductivities, κ_e for Mg_3Sb_2 and Mg_3Sb_2/GNS nanocomposites are displayed in Fig. 12(b). Obvious increases in the κ_e with GNS concentration for the nanocomposites were noted, owing to the increased electrical conductivities observed for the nanocomposites.

1   The temperature dependence of ZT of all the samples is calculated which is displayed in

2   Fig 13(a). The ZT of the nanocomposites increases with rising temperature as presented in Fig 13

3   (a). The maximum ZT ≈ 0.71 at temperature of 773 K for Mg_3Sb_2/GNS nanocomposite was

4   optimized for the mass ratio 80:1, which is significantly enhanced than ZT ≈ 0.26 at 773 K for

5   bare Mg_3Sb_2.[8] Thus combining a large increase (~130%) in the power factor due to significant

6   enhancement of electrical conductivity (~600%), along with 15% reduction in the thermal

7   conductivity at high temperature, the ZT of the nanocomposite with mass ratio 80:1 was

8   calculated to be about 170% larger than that of bare Mg_3Sb_2 sample.

9   Following similar strategy, GNS were also incorporated in a derivative of Mg_3Sb_2 with a

10   nominal composition $Mg_3Sb_{1.8}Bi_{0.2}$ to fabricate a nanocomposite of $Mg_3Sb_{1.8}Bi_{0.2}$/GNS and

11   thermoelectric properties were investigated. The optimized amount of GNS in the mass ratio of

12   80:1 was added. The temperature dependent behavior of all the thermoelectric parameters

13   followed consistently the similar trends. Interestingly, graphene incorporation in this case too,

14   leads to 650% improvement in the electrical conductivity, 90% improvement in the power factor

15   and 13% reduction in the thermal conductivity leading to a significant enhancement of ZT about

16   125% in comparison to that of $Mg_3Sb_{1.8}Bi_{0.2}$. Thus, graphene incorporation with its high mobility

17   in the present Zintl phase compound provides an emerging strategy to enhance the thermoelectric

18   performance of Mg_3Sb_2- based material. This strategy employed is summarized in fig. 13(b)

19   which clearly presents that large μ/κ_L value results higher ZT and this strategy of increasing

20   mobility by incorporating GNS in Mg_3Sb_2-based Zintl compound was successfully demonstrated

21   at room temperature. For this strategy to be effectively seen at higher temperature, high

22   temperature Hall measurement is required which will be future avenue of the research. We

23   believe that this strategy is not limited to only Mg_3Sb_2 based Zintl phase compound but may be

24   efficiently deployed for improving thermoelectric performance of other Zintl phase compounds

25   which are largely victim with the low electrical conductivity.

26   **Conclusion and Future Prospects:**

27   Novel $(Mg_3Sb_2, Mg_3Sb_{1.8}Bi_{0.2})$/GNS nanocomposites have been fabricated by

28   incorporating graphene nanosheets in pre-synthesized Mg_3Sb_2 and $Mg_3Sb_{1.8}Bi_{0.2}$ precursors

29   using wet mechanical milling and further rapid heating spark plasma sintering process. The

1   addition of small fraction of GNS into Mg_3Sb_2 and $Mg_3Sb_{1.8}Bi_{0.2}$ matrix resulted into the

2   significant enhancement in the electrical conductivity (~600% and ~650% respectively) and

3   thereby increasing to a large power factor (~130% and ~90% respectively) of thermoelectric

4   nanocomposites material. The thermal conductivity of the nanocomposites Mg_3Sb_2/GNS and

5     $Mg_3Sb_{1.8}Bi_{0.2}$/GNS at higher temperature are also decreased as compared to Mg_3Sb_2 and

6     $Mg_3Sb_{1.8}Bi_{0.2}$. Thus these nanocomposites outperform bare Mg_3Sb_2 and $Mg_3Sb_{1.8}Bi_{0.2}$ and attain

7   a ZT ~ 0.71 and a ZT ~ 1.35 at 773K respectively which are much larger than Mg_3Sb_2 (ZT ~

8   0.26) and $Mg_3Sb_{1.8}Bi_{0.2}$ (ZT ~ 0.6) materials. Since these materials are made from abundant and

9   non-toxic Mg, Sb and graphene and thus make them a cheap alternative and finds widespread use

10   over high scarcity and price of Te, Pb used in commercialized state-of-the-art thermoelectric

11   materials. A large boost in the electrical conductivity and reduced thermal conductivity at high

12   temperature in Mg_3Sb_2/GNS nanocomposite with mass ratio 80:1 suggests that there is plenty of

13   rooms for improvement of thermoelectric properties if a suitable concentration of GNS inclusion

14   is optimized. It may be anticipated that an optimal amount of GNS can further refined the size of

15   Mg_3Sb_2 particles and hence lattice thermal conductivity can be reduced for further boost in ZT of

16   such nanocomposites. Thus design of such nanocomposites combining Zintl phase with intrinsic

17   properties of PGEC for the potential thermoelectric materials with GNS appears to be a very

18   effective and promising path to be followed up for improving the thermoelectric properties. Off

19   course, this strategy is not unique to Mg_3Sb_2-based Zintl phase and may be extended to other

20   Zintl phase compounds possessing low electrical conductivity.

References:

1. G. Chen, M. S. Dresselhaus, G. Dresselhaus, J. P. Fleurial, T. Caillat, *Int. Mater. Rev.* **2003**, *48*, 45.

2. G. J. Snyder, E. S. Toberer, *Nat. Mater.* **2008**, *7*, 105.

3. J. Yang, H.-L. Yip, A. K.-Y. Jen, *Adv. Energy Mater.* **2013**, *3*, 549.

4. S. N. Girard, J. He, X. Zhou, D. Shoemaker, C. M. Jaworski, C. Uher, V. P. Dravid, J. P. Heremans, M. G. Kanatzidis, *J. Am. Chem. Soc.* **2011**, *133*, 16588.

5.   H. Wang, Y. Pei, A. D. LaLonde, G. J. Snyder, *Adv. Mater.* **2011**, *23*, 1366.

6. L. Pan, D. Bérardan, N. Dragoe, *J. Am. Chem. Soc.*, **2013**, *135*, 4914.

7.   H. Wang, A. D. LaLonde, Y. Pei, G. J. Snyder, *Adv. Func. Mater.* **2013**, *23*, 1586.

8. A. Bhardwaj, A. Rajput, A. K. Shukla, J. J. Pulikkotil, A. K. Srivastava, A. Dhar, G. Gupta, S. Auluck, D. K. Misra, R. C. Budhani, *RSC Adv.* **2013**, *3*, 8504.

9. C. Heinrich, T. Day, W. G. Zeier, G. J. Snyder, W. Tremel, *J. Am. Chem. Soc.* **2014**, *136*, 442.

10. X. Liu, H. Wang, L. Hu, H. Xie, G. Jiang, G. J. Snyder, X. Zhao, T. Zhu, *Adv. Energy Mater.* **2013**, *3*, 1238.

11. J.-F. Li, W.-S. Liu, L.-D. Zhao, M. Zhou, *NPG Asia Mater.* **2010**, *2*, 152.

12. D. K. Misra, A. Bhardwaj, S. Singh, *J. Mater. Chem.*, **2014**, 2, 11913- 11921

13. G. Joshi, X. Yan, H. Wang, W. Liu, G. Chen, Z. Ren, *Adv. Energy Mater.* **2011**, *1*, 643.

14. K. Nielsch, J. Bachmann, J. Kimling, H. Böttner, *Adv. Energy Mater.* **2011**, *1*, 713.

15. S. Sumithra, N. J. Takas, D. K. Misra, W. M. Nolting, P.F.P. Poudeu, K. L. Stokes, *Adv. Energy Mater.* **2011**, *1*, 1141.

16. A. Bhardwaj, D. K. Misra, J. J. Pulikkotil, S. Auluck, A. Dhar, R. C. Budhani, *Appl. Phys. Lett.* **2012**, *101*, 133103.

17. J. P. Heremans, V. Jovovic, E. S. Toberer, A. Saramat, K. Kurosaki, A. Charoenphakdee, A. Yamanaka and G. J. Snyder, *Science*, **2008**, 321, 554.

18. S. Y. Wang, X. J. Tan, G. J. Tan, X. Y. She, W. Liu, H. Li, H. J. Liu and X. F. Tang, *J. Mater. Chem.*, **2012**, 22, 13977.

19. Y. Z. Pei, X. Y. Shi, A. LaLonde, H. Wang, L. D. Chen and G. J. Snyder, *Nature*, **2011**, 473, 66.

20. W. Liu, X. J. Tan, K. Yin, H. J. Liu, X. F. Tang, J. Shi, Q. J. Zhang and C. Uher, *Phys. Rev. Lett.*, **2012**, 108, 166601.

21. B. Paul, V. A. Kumar and P. Banerji, *J. Appl. Phys.*, **2006**, 108, 064322.

22. B. Poudel, Q. Hao, Y. Ma, Y. Lan, A. Minnich, B. Yu, X. Yan, D. Wang, A. Muto, D. Vashaee, X. Chen, J. Liu, M. S. Dresselhaus, G. Chen, Z. Ren, *Science* **2008**, *320*, 634.

23. S. Yu, J. Yang, Y. Wu, Z. Han, J. Lu, Y. Xie, Y. Qian, *J. Mater. Chem.* **1998**, *8*, 1949.

24. J. Shen, T. Zhu, X. Zhao, S. Zhang, S. Yanga, Z. Yina, *Energy Environ. Sci.* **2010**, *3*, 1519.

25. M. E. Anderson, S. S. N. Bharadwaya, R. E. Schaak, *J. Mater. Chem.* **2010**, *20*, 8362.

26. S. Sumithra, N. J. Takas, D. K. Misra, W. M. Nolting, P. F. P. Poudeu, K. L. Stokes, *Adv. Energy Mater.* **2011**, *1*, 1141.

27. K. F. Hsu, S. Loo, F. Guo, W. Chen, J. S. Dyck, C. Uher, T. Hogan, E. K. Polychroniadis, M. G. Kanatzidis, *Science* **2004**, *303*, 818.

28. J. Androulakis, K. F. Hsu, R. Pcionek, H. Kong, C. Uher, J. J. D'Angelo, A. Downey, T. Hogan, M. G. Kanatzidis, *Adv. Mater.* **2006**, *18*, 1170.

29. J. R. Sootsman, H. Kong, C. Uher, J. J. D'Angelo, C. I. Wu, T. P. Hogan, T. Caillat, M. G. Kanatzidis, *Angew. Chem.* **2008**, *47*, 8618.

30. K. Ahn, K. Biswas, J. He, I. Chung, V. Dravid, M. G. Kanatzidis, ***Energy Environ. Sci.*** **2013**, *6*, 1529.

31. R. Basu, S. Bhattacharya, R. Bhatt, M. Roy, S. Ahmad, A. Singh, M. Navaneethan, Y. Hayakawa, D. K. Aswal, S. K. Gupta, *J. Mater. Chem. A* **2014**, *2*, 6922.

32. G. Joshi, H. Lee, Y. Lan, X. Wang, G. Zhu, D. Wang, R. W. Gould, D. C. Cuff, M. Y. Tang, M. S. Dresselhaus, G. Chen, Z. F. Ren, *Nano Lett.* **2008**, *8*, 4670.

33. E. S. Toberer, C. A. Cox, S. R. Brown, T. Ikeda, A. F. May, S. M. Kauzlarich and G. J. Snyder *Adv. Funct. Mater.* 2008, 18, 2795.

34. A. Bhardwaj and D. K. Misra, *RSC Adv.*, 2014, **4**, 34552.

35. S. R. Brown, S. M. Kauzlarich, F. Gascoin, G. J. Snyder, *Chem. Mater.* **2006**, *18*, 1873.

36. G. J. Snyder, M. Christensen, E. Nishibori, T. Caillat, B. B. Iversen, *Nature Mater.* **2004**, *3*, 458.

37. S. K. Bux, A. Zevalkink, O. Janka, D. Uhl, S. Kauzlarich, J. G. Snyder, J. P. Fleurial, *J. Mater. Chem. A* **2014**, *2*, 215.

38. B. C. Sales, D. Mandrus, R. K. Williams, *Science* **1996**, *272*, 1325.

39. J. W. Graff, X. Zeng, A. M. Dehkordi, J. He and T. M. Tritt, *J. Mater. Chem. A* **2014**, *2*, 8933.

40. G. S. Nolas, J. L. Cohn, G. A. Slack, S. B. Schujman, *Appl. Phys. Lett.* **1998**, *73*, 178.

41. H. Kleinke, *Chem. Mater.* **2010**, *22*, 604.

42. F. Gascoin, S. Ottensmann, D. Stark, S. M. Haile, G. J. Snyder, *Adv. Funct. Mater.* **2005**, 15, 1860.

43. X. J. Wang, M. B. Tang, J. T. Zhao, H. H. Chen, X. X. Yang, *Appl. Phys. Lett.* **2007**, *90*, 232107.

44. X. J. Wang, M. B. Tang, H. H. Chen, X. X. Yang, J. T. Zhao, U. Burkhardt, Y. Grin, *Appl. Phys. Lett.* **2009**, *94*, 092106.

45. S. J. Kim, M. G. Kanatzidis, *Inorg. Chem.* **2001**, *40*, 3781.

46. S. M. Park, E. S. Choi, W. Kang, S. J. Kim, *J. Mater. Chem.* **2002**, *12*, 1839.

47. S. J. Kim, J. R. Ireland, C. R. Kannewurf, M. G. Kanatzidis, *J. Solid State Chem.* **2000**, *155*, 55.

48. H. Zhang, J. T. Zhao, Y. Grin, X. J. Wang, M. B. Tang, Z. Y. Man, H. H. Chen, X. X. Yang, *J. chem. Phys.* **2008**, *129*, 164713.

49. G. S. Pomrehn, A. Zevalkink, W. G. Zeier, A. van de Walle, G. J. Snyder, *Angew. Chem. Int. Ed.* **2014**, *53*, 3422.

50. K. S. Novoselov, D. Jiang, F. Schedin, T. J. Booth, V. V. Khotkevich, S. V. Morozov, A. K. Geim, *Proc. Natl. Acad. Sci. U. S. A.* **2005**, *102*, 10451.

51. Y. Zhang, Y.-W. Tan, H. L. Stormer and P. Kim, *Nature* **2005**, *438*, 201.

52. D. A. Abanin, S. V. Morozov, L. A. Ponomarenko, R. V. Gorbachev, A. S. Mayorov, M. I. Katsnelson, K. Watanabe, T. Taniguchi, K. S. Novoselov, L. S. Levitov, A. K. Geim, *Science* **2011**, *332*, 328.

1   53. J. H. Seol, I. Jo, A. L. Moore, L. Lindsay, Z. H. Aitken, M. T. Pettes, X. Li, Z. Yao, R.

2   Huang, D. Broido, N. Mingo, R. S. Ruoff, L. Shi, *Science* **2010**, *328*, 213.

3   54. A. K. Geim, K. S. Novoselov, *Nat. Mater.* **2007**, *6*, 183.

4   55. C. N. R. Rao, K. Biswas, K. S. Subrahmanyam, A. Govindaraj, *J. Mater. Chem.* **2009**, *19*,

5   2457.

6   56. K. S. Novoselov, A. K. Geim, S. V. Morozov, D. Jiang, Y. Zhang, S. V. Dubonos, I. V.

7   Grigorieva, A. A. Firsov, *Science* **2004**, *306*, 666.

8   57. A. V. Murugan, T. Muraliganth, A. Manthiram, *Chem. Mater.* **2009**, *21*, 5004.

9   58. Z. S. Wu, W. C. Ren, D. W. Wang, F. Li, B. L. Liu, H. M. Cheng, *Am. Chem. Soc. Nano*

10   **2010**, *4*, 5835.

11   59. K. S. Novoselov, A. K. Geim, S. V. Morozov, D. Jiang, M. I. Katsnelson, I. V. Grigorieva, S.

12   V. Dubonos, A. A. Firsov, *Nature* **2005**, *438*, 197.

13   60. B. Seger, P. V. Kamat, *J. Phys. Chem. C* **2009**, *113*, 7790

14   61. S. Stankovich, D. A. Dikin, G. H. B. Dommett, K. M. Kohlhaas, E. J. Zimney, E. A. Stach,

15   R. D. Piner, S. T. Nguyen and R. S. Ruoff, *Nature* **2006**, *442*, 282.

16   62. J. W. Zhu, G. Y. Zeng, F. D. Nie, X. M. Xu, S. Chen, Q. F. Han, X. Wang, *Nanoscale* **2010**,

17   *2*, 988.

18   63. R. Pasricha, S. Gupta, A. K. Srivastav, *Small* **2009**, *5*, 2253.

19   64. J. Dong, W. Liu, H. Li, X. Su, X. Tang and C. Uher, *J. Mater. Chem. A*, **2013**, 1, 12503

20   65. H. Chen, C. Yang, H. Liu, G. Zhang, D. Wan, F. Huang, *Cryst. Engg. Comm.* **2013**, 15,

21   6648.

22   66. B. Liang, Z. Song, M. Wang, L. Wang, and W. Jiang, *J. of Nanomaterials,* **2013**, 2013, 5.

23   67. L. Wang, F. Liu, C. Jin, T. Zhang and Q. Yin, *RSC Adv.*, **2014**, 4, 46187-46193

24   68. B. Feng, J. Xie, G. Cao, T. Zhu and X. B. Zhao, *J. Mater. Chem. A,* **2013**, 1, 13111-13119

25   69. G. A. Slack, *In CRC Handbook of Thermoelectrics*, CRC, New York, 1995.

26   70. S. M. Kauzlarich, *Chemistry, Structure, and Bonding of Zintl Phases and Ions*, VCH

27   Publishers, New York, 1996.

28   71. S. M. Kauzlarich, S. R. Brown, G. J. Snyder, *Dalton Trans.* **2007**, *113*, 2099.

29   72. A. M. Mills, R. Lam, M. J. Ferguson, L. Deakin, A. Mar, *Coord. Chem. Rev.* **2002**, *233*, 207.

30   73. G. A. Slack, *Solid State Phys.* Academic Press, New York, 1979.

74. E. S. Toberer, A. Zevalkink, G. J. Snyder, *J. Mater. Chem.* **2011**, *21*, 15843.

75. M. M. Ripoll, A. Haase, G. Brauer, *Acta Cryst.* **1974**, *B30*, 2006.

76. J. H. Slowik, *Phys. Rev. B* **1974**, *10*, 416.

77. L. M. Watson, C. A.W. Marshall, C. P. Cardoso, *J. Phys. F: Met. Phys.* **1984**, *14*, 113.

78. C. Zheng, R. Hoffmann, R. Nesper, H. G. von Schnering, *J. Am. Chem. Soc.* **1986**, *108*, 1876.

79. S. R. Dhakate, S. Sharma, M. Borah, R. B. Mathur, T. L. Dhami, *Inter J. Hydrogen Energy* **2008**, *33*, 7146.

80. T. Gupta, B. P. Singh, R. B. Mathur, S. R. Dhakate, *Nanoscale,* **2014**, *6*, 842.

81. M. Borah, M. Dahiya, S. Sharma, R. B. Mathur, S. R. Dhakate, *Mater. Focus,* **2014**, 3, 300-309.

82. F. Schedin, A. K. Geim, S. V. Morozov, E. W. Hill, P. Blake, M. I. Katsnelson, K. S. Novoselov, *Nat. Mater.* **2007**, *6*, 652.

83. Z. J. Fan, W. Kai, J. Yan, T. Wei, L.-J. Zhi, J. Feng, Y.-M. Ren, L. P. Song, F. Wei, *ACS Nano*, **2011**, 5, 191.

84. J. Zhou, H. Song, L. Ma and X. Chen, *RSC Adv.*, **2011**,1, 782.

85. V. G. Kravets, R. Jalil, Y.-J. Kim, D. Ansell, D. E. Aznakayeva, B. Thackray, L. Britnel, F. Withers, I. P. Radko, Z. Han, S. I. Bozhevolnyi, K. S. Novoselov, A. K. Geim, B. D. Belle, A. N. Grigorenko, *Scientific Reports*, **2014**, 4, 4237.

86. M. J. Webb, P. Palmgren, P. Pal, O. Karis, H. Grennberg, *Carbon*, **2011**, 49, 3242.

87. C. H. A. Wong, M. Pumera, *J. Mater. Chem. C*, **2014**, 2, 856.

88. M. –C. Hsiao, S. –H. Liao, M. –Y. Yen, C. –C. Teng, S. –H. Lee, N. –W. Pu, C. –A. Wang, Y. Sung, M. –D. Ger, C. –C. M. Ma, M. –H. Hsiao, *J. Mater. Chem.*, **2010**, 20, 8496.

89. V. Johnson and K. Lark-Horovitz, Phys. Rev., 1953, 92, 226.

90. A. Bhardwaj and D. K. Misra, J. Mater. Chem. A, 2014, 2, 20980-20989

91. H. Kitagawa, M. Wakatsuki, H. Nagaoka, H. Noguchi, Y. Isoda, K. Hasezaki, Y. J. Noda, *Phys. Chem. Solids* **2005**, *66*, 1635.

92. W. S. Liu, B. P. Zhang, J J. F. Li, H. L. Zhang, L. D. Zhao, *J. Appl. Phys.* **2007**, *102*, 103717.

1 **Figure Caption:**

2 **Figure 1.** (a) X-ray diffraction (XRD) pattern of Mg_3Sb_2/GNS nanocomposites with mass ratio

3 of 100:1,80:1, 60:1, 40:1 and for $Mg_3Sb_{1.8}Bi_{0.2}$/GNS with 80:1. Inset of fig 1(a) shows the

4 Schematic diagram of layered crystal structure of Mg_3Sb_2 showing the anionic framework of

5 $[Mg_2Sb_2]^{2-}$ with double layer and Mg^{2+} cations between the layers. (b) Shows the TEM image of

6 reduced GNS. Inset (fig 1b) shows the XRD of the reduced GNS. (c) HRTEM image of GNS

7 indicating excellent crystallinity.

8 **Figure 2:** Shows the Raman spectra of graphene nanosheets (black color spectra) and

9 Mg_3Sb_2/GNS nanocomposites for mass ratio 80:1(green color spectra). Inset shows the spectra

10 for Mg_3Sb_2.

11 **Figure** 3: XPS survey spectrum of pure GNS, bare Mg_3Sb_2 and Mg_3Sb_2/GNS nanocomposites

12 over wide binding energy range. All the features in the spectra have been identified. All the

13 spectra have been staggered vertically for clarity of presentation.

14 **Figure 4**: C 1s core level spectra for GNS (bottom) and Mg_3Sb_2/GNS (80:1) (top). Experimental

15 data (open circles), fitted spectra (thick solid line) and deconvoluted fitting components (shaded

16 region) are also shown.

17 **Figure 5**: Mg 1s (left panel) and Sb 3d (right panel) core level spectra for bare Mg_3Sb_2 and

18 nanocomposite Mg_3Sb_2/GNS (80:1). All the spectra have been normalized to peak height for

19 comparison and were staggered vertically for clarity of presentation. Dashed line tracks the

20 binding energy position.

21 **Figure 6**: XPS valence band spectra for bare Mg_3Sb_2 and nanocomposite Mg_3Sb_2/GNS (80:1).

22 Inset shows the near Fermi level (E_F) region. Straight lines (thick solid lines) show fitting of

23 leading edge and background. Vertical dashed lines show the position of valence band maxima

24 (VBM). Shaded area (patterned) represents density of states between VBM and E_F.

25 **Figure 7:** (a) The SEM image of Mg_3Sb_2 showing homogeneous polycrystalline grains. (b)

26 Energy dispersive X-ray spectrum (EDAX) of Mg_3Sb_2 indicating (inset fig. 7b) the presence of

27 Mg and Sb and quantification results to the composition of Mg_3Sb_2 phase. (c & d) Magnified FE-

1   SEM image of Mg_3Sb_2/GNS nanocomposite with mass ratio 80:1 showing uniformly anchored

2   Mg_3Sb_2 particles on the graphene nanosheets (e) The SEM-EDAX analysis of Mg_3Sb_2/GNS

3   nanocomposite with mass ratio 80:1showing presence of Mg_3Sb_2 with graphene.

4   **Figure 8.** a) TEM image obtained from the specimen of Mg_3Sb_2 showing highly densified grains

5   b) SAED pattern corresponding to Mg_3Sb_2, revealing β-Mg_3Sb_2-type hexagonal structure, c) The

6   HRTEM   image of Mg_3Sb_2 exhibiting the presence of different orientations of the

7   crystallographic planes and their interface boundaries. d) EDAX spectrum recorded from

8   Mg_3Sb_2, confirms the composition of Mg_3Sb_2.

9   **Figure 9:** a) TEM image of Mg_3Sb_2/GNS (80:1) nanocomposite showing uniformly anchoring of

10   Mg_3Sb_2 particles on the surface of graphene nanosheets. (b-c) Magnified TEM images of

11   Mg_3Sb_2/GNS (80:1) nanocomposite showing more clearly the anchored Mg_3Sb_2 particles on to

12   the sheet of graphene nanosheets and the inset (fig. 9c) show an orientational relationship

13     $(002)GNS//(101)Mg_3Sb_2$ between the two phase. (d) HRTEM images of Mg_3Sb_2/GNS (80:1)

14   nanocomposite showing only Mg_3Sb_2 grains, no GNS was resolved at such high magnification.

15   (f) Schematic diagram of reaction mechanism occurred during the fabrication of Mg_3Sb_2/GNS

16   nanocomposite.

17   **Figure 10:** Temperature dependence of Electrical conductivity of Mg_3Sb_2/GNS nanocomposite

18   with mass ratio 100:1, 80:1, 60:1, 40:1 and for $Mg_3Sb_{1.8}Bi_{0.2}$/GNS nanocomposites with mass

19   ratio 80:1.

20   **Figure 11:** Temperature dependence of (a) Seebeck coefficient and (b) power factor of

21   Mg_3Sb_2/GNS nanocomposites with mass ratio of 100:1, 80:1, 60:1, 40:1 and for

22 $Mg_3Sb_{1.8}Bi_{0.2}$/GNS nanocomposite with mass ratio 80:1.

23   **Figure 12:** Temperature dependence of (a) Thermal conductivity (κ), (b) Electronic thermal

24   conductivity (κ_e) and (C) lattice thermal conductivity (κ_L) of Mg_3Sb_2/GNS nanocomposites with

25   mass ratio of 100:1,80:1, 60:1, 40:1 and for $Mg_3Sb_{1.8}Bi_{0.2}$/GNS with 80:1.

26   **Figure 13:** (a) Temperature dependence of thermoelectric figure of merit (ZT) of Mg_3Sb_2/GNS

27   nanocomposites with mass ratio of 100:1, 80:1, 60:1, 40:1 and for $Mg_3Sb_{1.8}Bi_{0.2}$/GNS
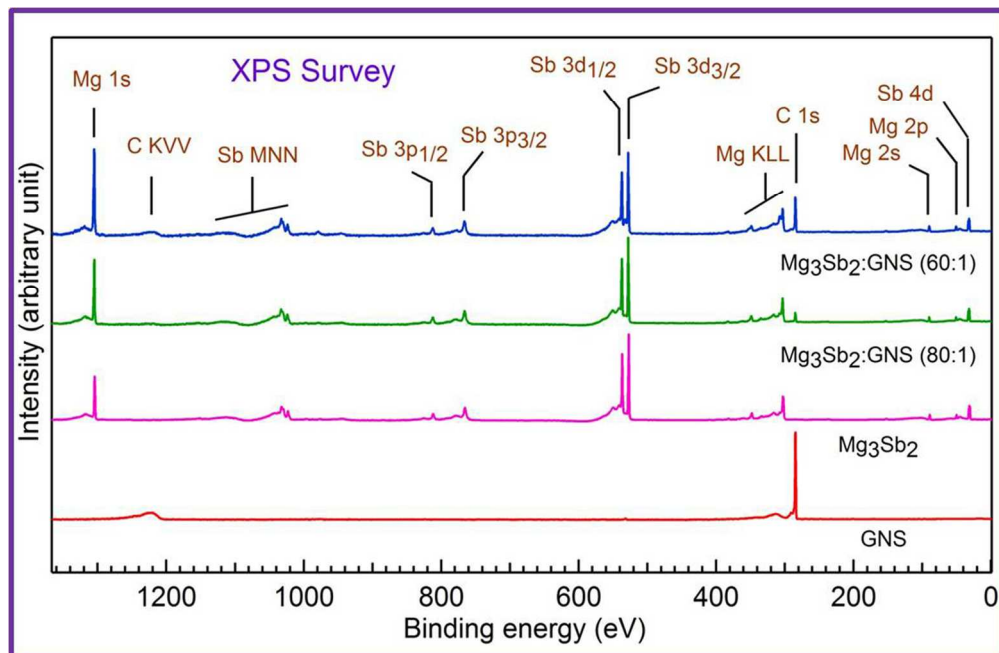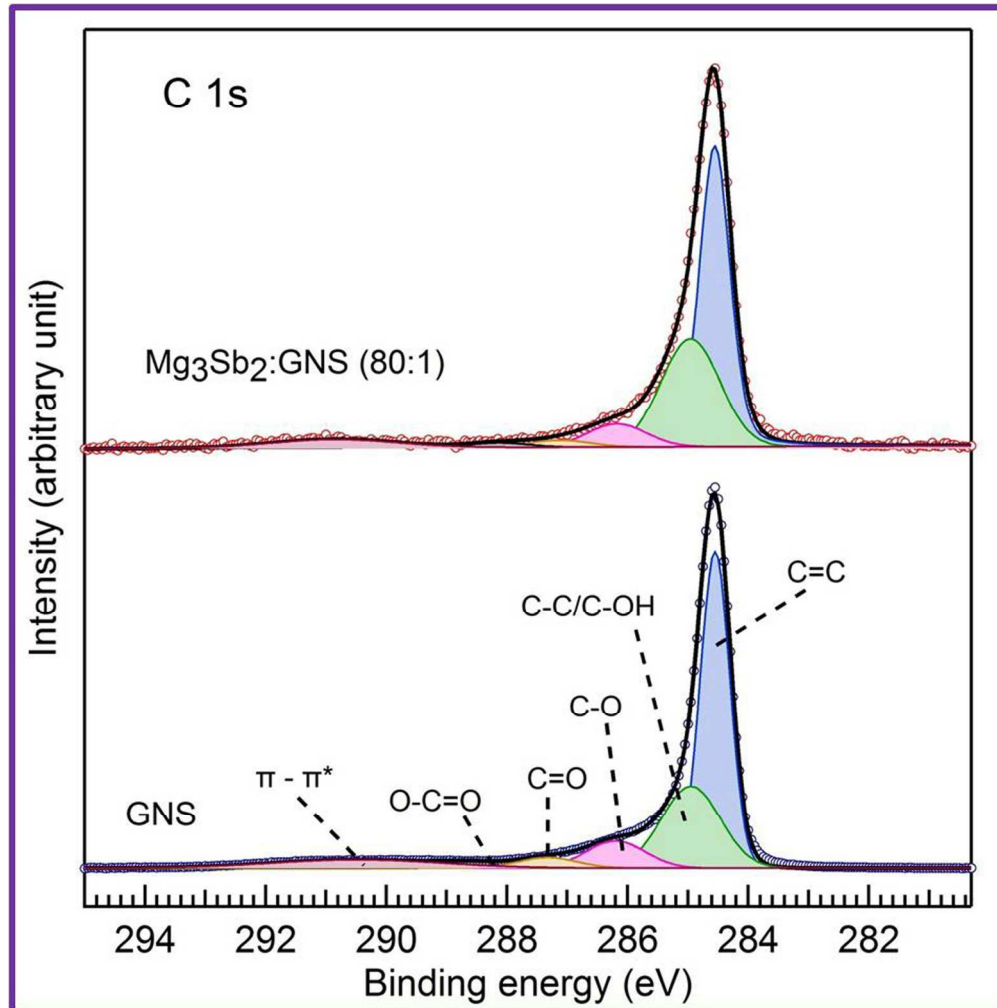
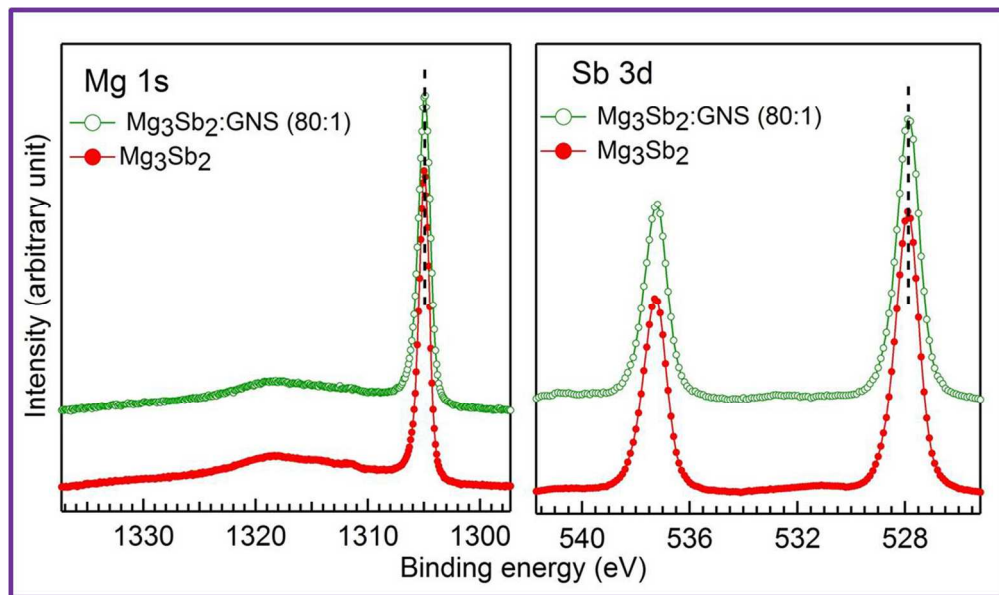28   nanocomposites with mass ratio of 80:1.
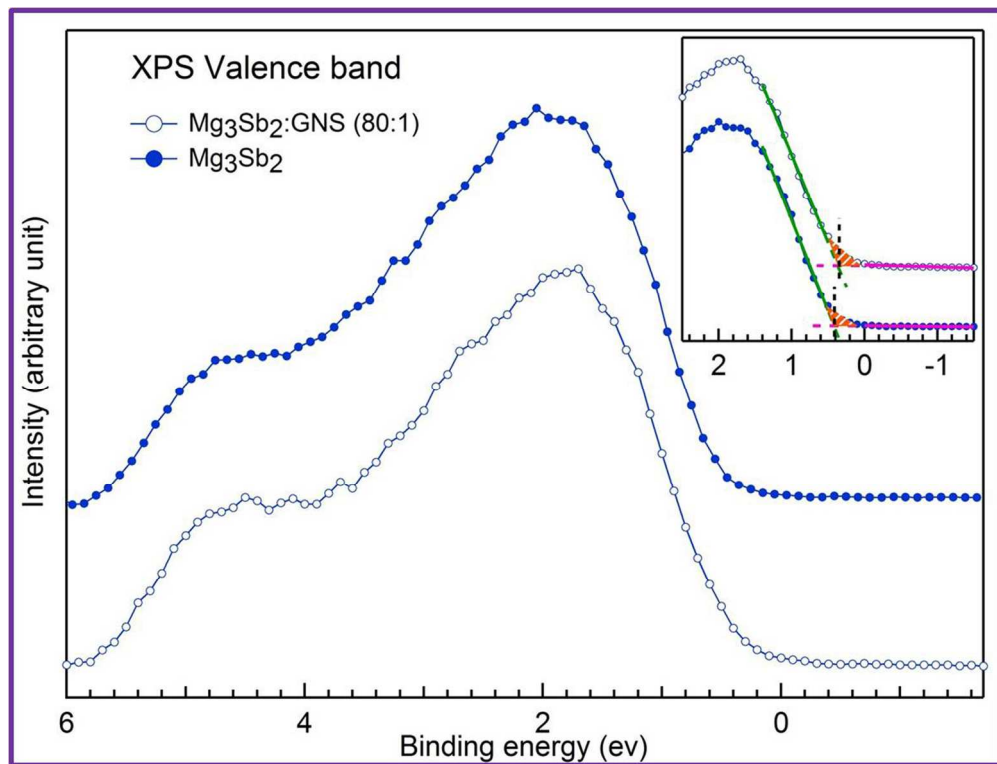
1
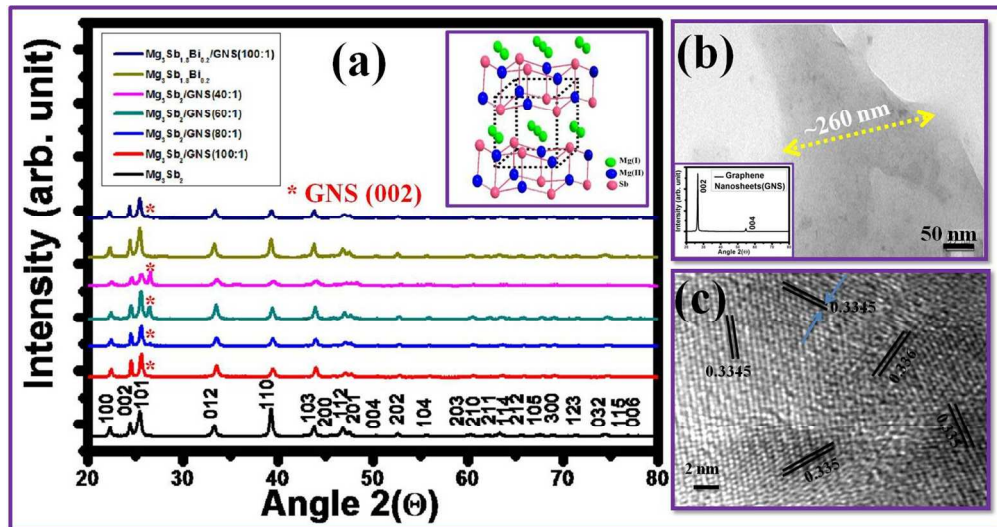
260x137mm (150 x 150 DPI)
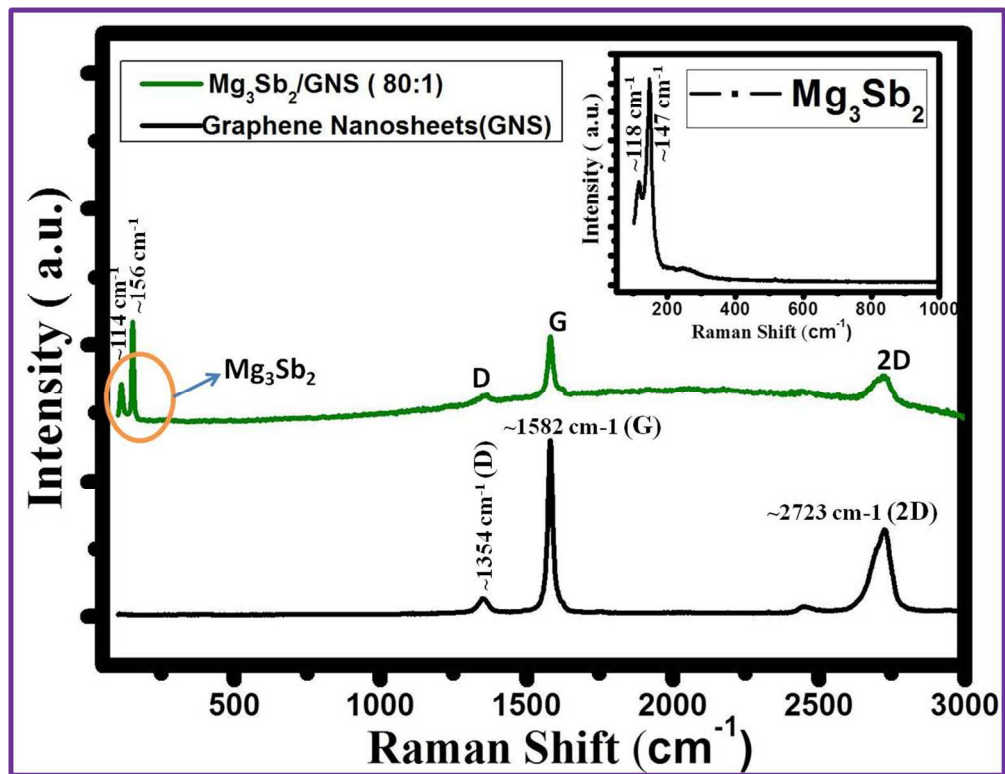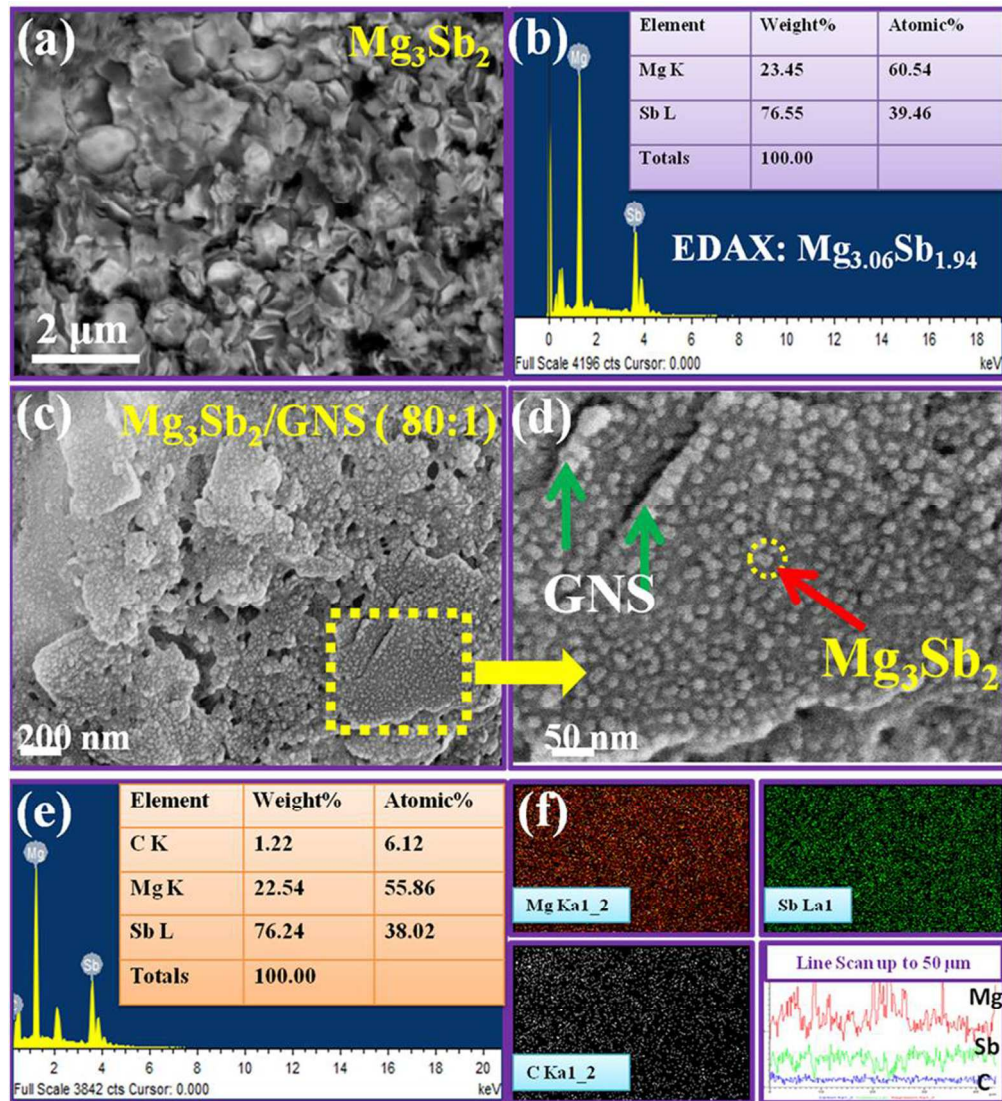
209x161mm (150 x 150 DPI)
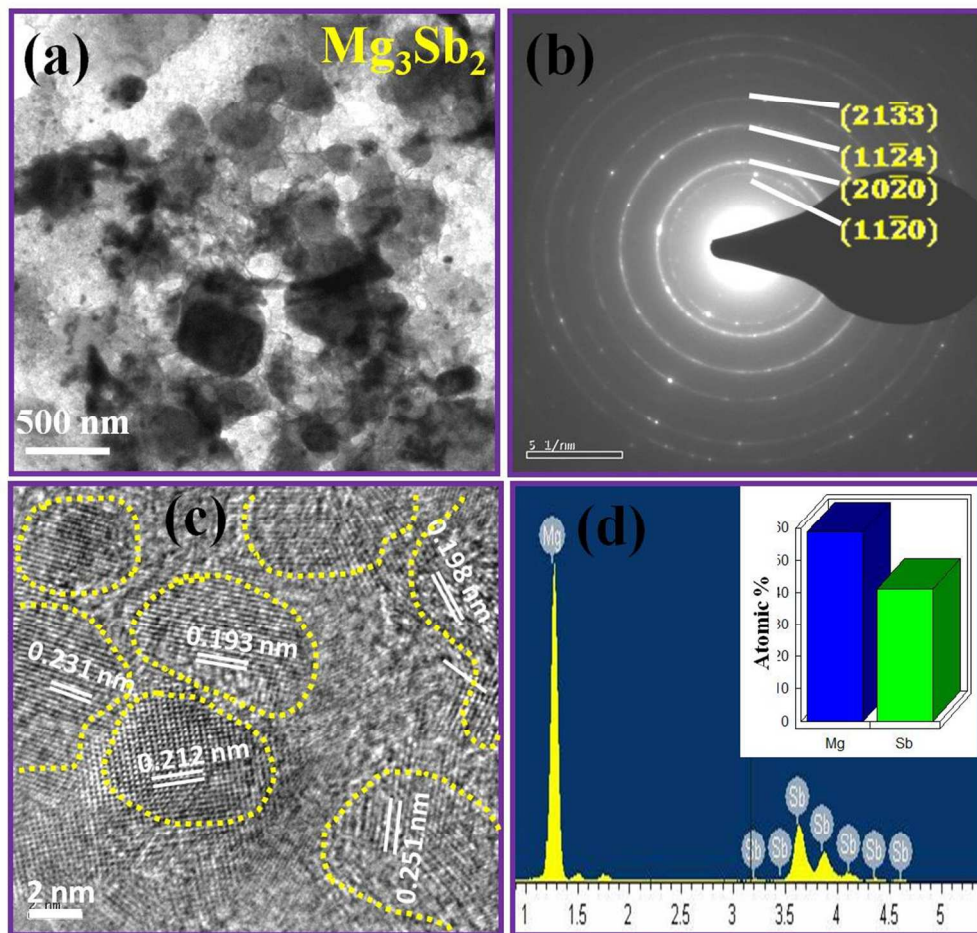
127x83mm (300 x 300 DPI)
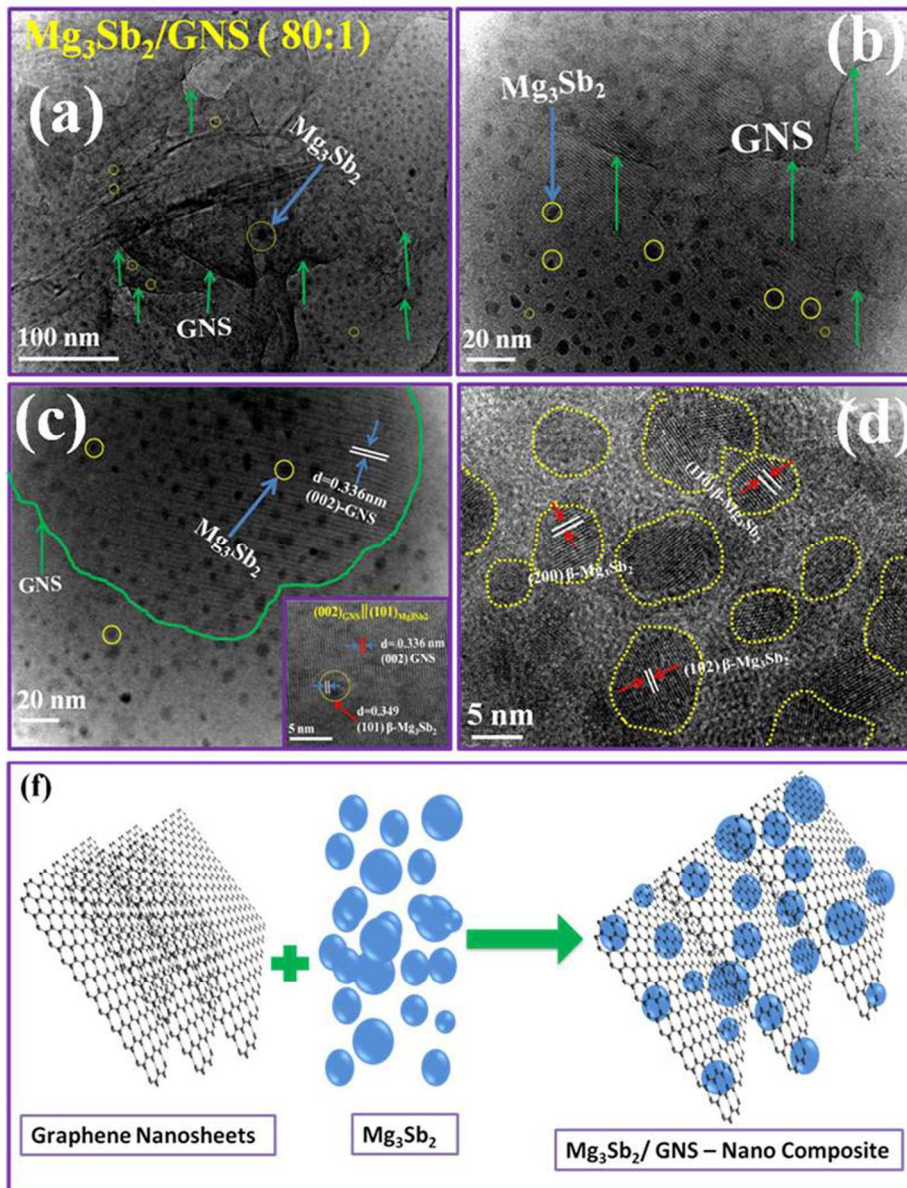
163x165mm (300 x 300 DPI)

131x77mm (300 x 300 DPI)

153x116mm (300 x 300 DPI)
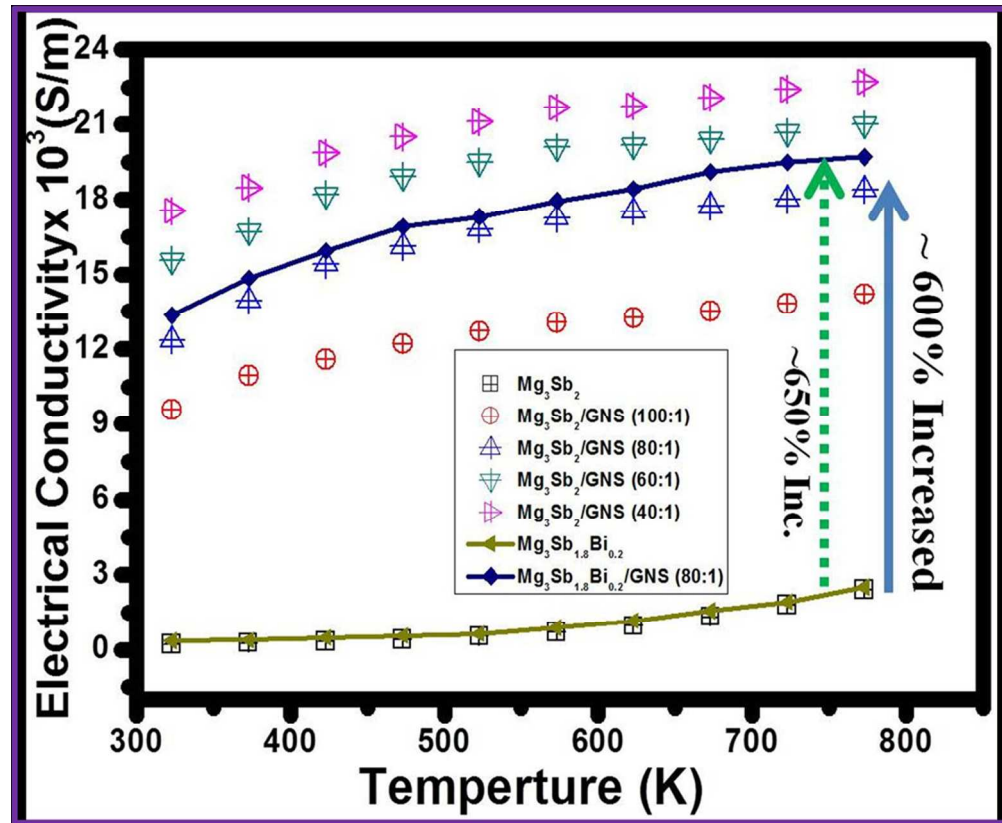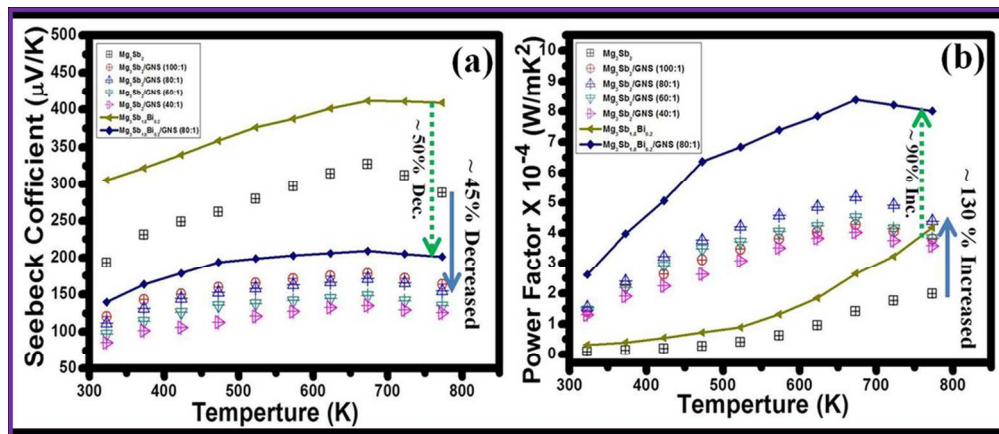
188x208mm (300 x 300 DPI)

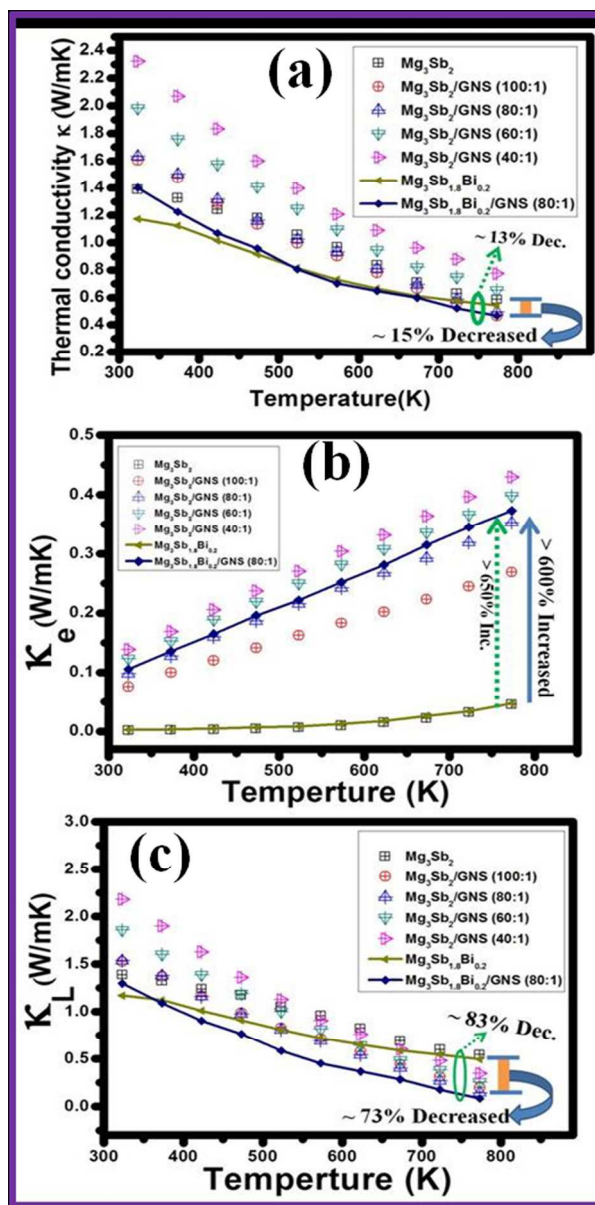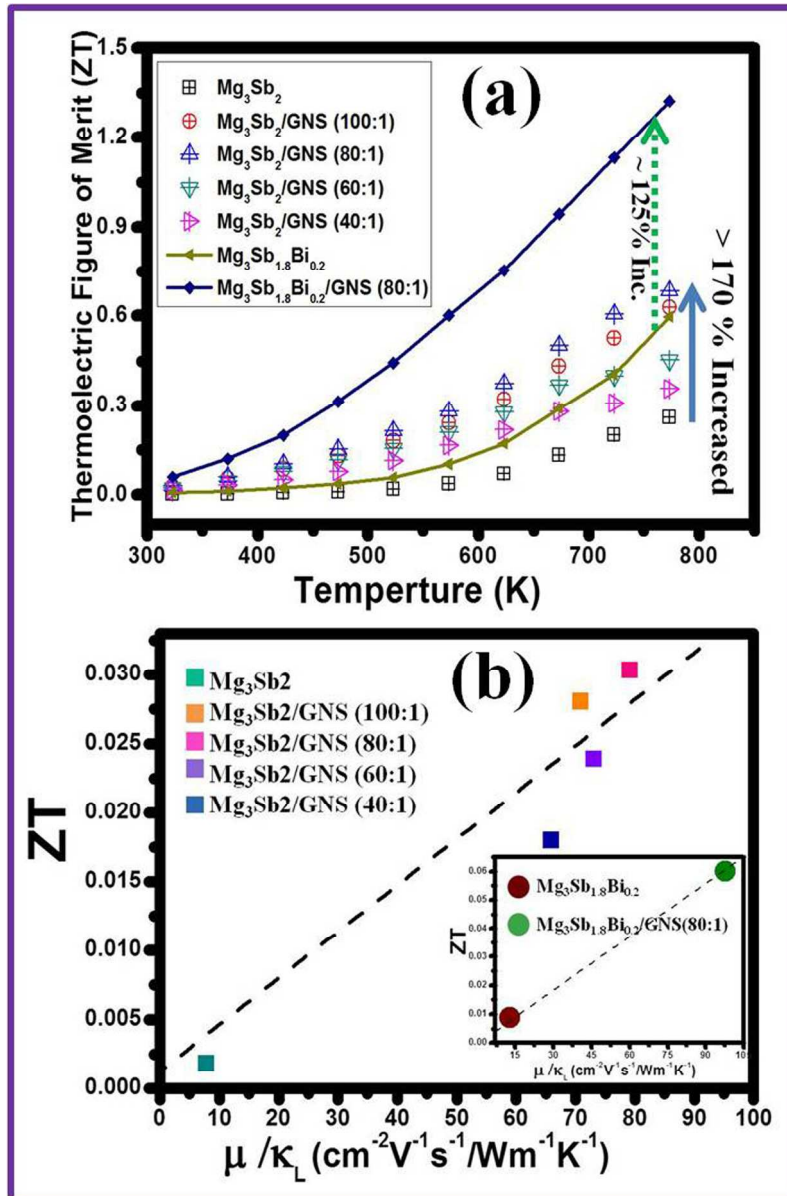191x180mm (150 x 150 DPI)

177x231mm (300 x 300 DPI)

145x119mm (300 x 300 DPI)

101x43mm (300 x 300 DPI)

179x359mm (300 x 300 DPI)

183x277mm (300 x 300 DPI)

Table1. Showing composition and various physical parameters

S.No.	Nominal Composition	Actual Composition (SEM-EDAX)	Electrical Conductivity σ (10^3 Sm^{-1})	Hall Coefficient R_H (10^{-2} cm^{3}C^{-1})	Carrier conc. n (10^{20} cm^{-3})	Mobility μ (cm^{2}V^{-1}s^{-1})	Seebeck Coefficient α (μV/K)
1.	Mg_3Sb_2	$Mg_{60.54}Sb_{39.46}$	0.206	5.02	1.2	11	193.2
2.	Mg_3Sb_2/GNS (100:1)	$C_{4.87}Mg_{56.94}Sb_{38.29}$	9.61	1.01	5.3	108.3	120.39
3.	Mg_3Sb_2/GNS (80:1)	$C_{6.12}Mg_{55.86}Sb_{38.02}$	12.35	0.98	6.1	121.7	111.41
4.	Mg_3Sb_2/GNS (60:1)	$C_{8.41}Mg_{54.68}Sb_{36.91}$	15.56	0.87	6.9	135.9	97.02
5.	Mg_3Sb_2/GNS (40:1)	$C_{11.38}Mg_{52.49}Sb_{35.13}$	17.49	0.82	7.3	144	85.71
6.	$Mg_3Sb_{1.8}Bi_{0.2}$	$Mg_{59.92}Sb_{36.45}Bi_{3.03}$	0.358	4.28	1.4	15.1	305.43
7.	$Mg_3Sb_{1.8}Bi_{0.2}$/GNS (80:1)	$C_{7.12}Mg_{54.51}Sb_{33.26}Bi_{5.11}$	13.35	0.95	6.3	126.8	139.78